nature nanotechnology

Article

https://doi.org/10.1038/s41565-025-01940-1

Atomic manipulation of the emergent quasi-2D superconductivity and pair density wave in a kagome metal

Received: 26 September 2024

Accepted: 17 April 2025

Published online: 10 June 2025

Check for updates

Xianghe Han[1,2,5], Hui Chen[1,2,5] ✉, Hengxin Tan[3], Zhongyi Cao[1,2], Zihao Huang[1,2], Yuhan Ye[1,2], Zhen Zhao[1,2], Chengmin Shen[1,2], Haitao Yang[1,2], Binghai Yan[3], Ziqiang Wang[4] ✉ & Hong-Jun Gao[1,2] ✉

The unconventional charge density wave (CDW) order in layered kagome lattice superconductors AV_3Sb_5 (A = K, Cs or Rb) triggers the emergence of novel quantum states such as time-reversal symmetry breaking and electronic liquid crystal states. However, atomic-scale manipulation and control of such phases remains elusive. Here we observe the emergent superconductivity and a primary pair density wave at the 2 × 2 Cs reconstructed surface of CsV_3Sb_5 by means of low-temperature scanning tunnelling microscopy/spectroscopy paired with density functional theory calculations. This quasi-two-dimensional kagome superconducting state with a critical temperature of ~5.4 K is intertwined with the bulk CDW order and exhibits a unique vortex core spectrum and a 4 × 4 pair density wave modulation of the superconducting gap. The emergent phenomena happen at a π-phase-shift dislocation in the periodicity of the CDW along the stacking direction if the 2 × 2 Cs superstructures are out of phase with the bulk CDW. Furthermore, we switched on and off the quasi-two-dimensional superconductivity through tip-assisted atomic manipulation of the 2 × 2 Cs superstructure. Thus, control of the surface reconstruction permits the creation, manipulation and control of quantum many-body states at antiphase boundaries in kagome lattice superconductors and, potentially, in other correlated materials.

Vanadium-based kagome metals AV_3Sb_5 (A = K, Cs or Rb) exhibit rich quantum phases[1–4], which may be manipulated at the atomic scale. The AV_3Sb_5 single crystals have a layered structure containing two-dimensional (2D) kagome lattice planes formed by V atoms[5,6] (Fig. 1a). In contrast to the insulating[7] and itinerant magnetic[8,9] transition-metal kagome materials, AV_3Sb_5 compounds are non-magnetic and have a superconducting ground state[5,10]. They possess a cascade of symmetry breaking correlated and topological quantum states, in addition to the charge density wave (CDW) order[11–14]. Apart from the broken lattice translation symmetry, some works indicates that rotation symmetry is broken in an intricate manner[15], exhibiting a rich set of electronic liquid crystal states such as smectic order[16–18], stripes[19,20] and electronic nematicity[21–23]. There is some experimental evidence for a spontaneous time-reversal symmetry breaking[24–26] CDW state, which is unexpected and non-trivial in the absence of spin magnetism and is under intensive debate[17,27,28]. These many-body states transition to a superconducting state at low temperatures, exhibiting evidence for time-reversal symmetry breaking[29,30], pair density

[1]Beijing National Center for Condensed Matter Physics and Institute of Physics, Chinese Academy of Sciences, Beijing, People's Republic of China. [2]School of Physical Sciences, University of Chinese Academy of Sciences, Beijing, People's Republic of China. [3]Department of Condensed Matter Physics, Weizmann Institute of Science, Rehovot, Israel. [4]Department of Physics, Boston College, Chestnut Hill, MA, USA. [5]These authors contributed equally: Xianghe Han, Hui Chen. ✉e-mail: hchenn04@iphy.ac.cn; wangzi@bc.edu; hjgao@iphy.ac.cn

https://doi.org/10.1038/s41565-025-01940-1

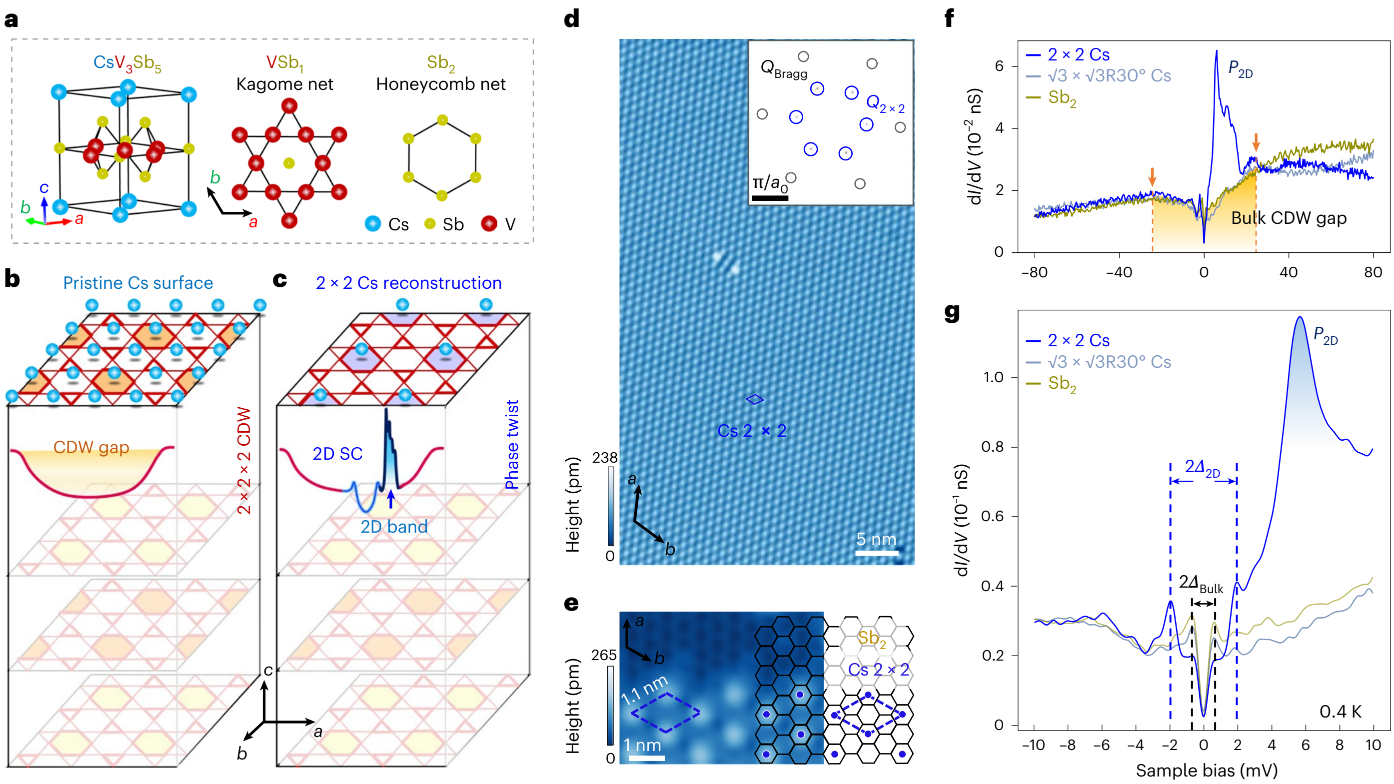

Fig. 1 | Emergent low-energy gap and incipient surface band inside the bulk CDW gap on the 2 × 2 Cs ordered surface of CsV_3Sb_5. **a**, The atomic structure of CsV_3Sb_5, featuring a stratified composition of VSb sheets intercalated by Cs. Within the VSb1 plane, the V atoms arrange in a kagome net, entwined with a hexagonal net formed by the Sb1 atoms. The Cs atoms sit right above the Sb1 atoms, forming a hexagonal lattice. The Sb2 layer forms a honeycomb lattice. **b**, A schematic of the pristine Cs surface of CsV_3Sb_5, showing the bulk CDW gap. **c**, A schematic of the 2 × 2 ordered Cs surface of CsV_3Sb_5, showing the emergence of a quasi-2D superconducting (SC) gap and a narrow band of bound states when the 2 × 2 Cs order is out of phase with the bulk CDW. **d**, The STM topography of as-cleaved CsV_3Sb_5 at low temperature showing a large area of 2 × 2 ordered superlattice structure (V_{set} = 900 mV, I_t = 50 pA). The black arrows highlight the two crystalline directions. The blue rhombus highlights the unit cell of 2 × 2 Cs reconstruction. The inset shows the FT of the STM topography, showing the $\boldsymbol{Q}_{2\times2}$ (blue circles) and $\boldsymbol{Q}_{Bragg}$ (black circles). **e**, STM topography and schematic of the 2 × 2 Cs (dashed blue rhombus) and Sb surface regions, showing the atomic configuration of Cs atoms (blue spots) on the honeycomb lattice of the Sb2 layer (black hexagons). V_{set} = 40 mV, I_t = 1 nA. **f**,**g**, The spatially averaged dI/dV spectra obtained on different surfaces of CsV_3Sb_5 at a temperature of 0.4 K in the voltage range of −80 to 80 mV (**f**) and −10 to 10 mV (**g**), showing the emergence of a series of narrow bands of bound sates with the sharpest spectral peak around 5.6 mV (P_{2D}) inside the bulk CDW gap (highlighted by the orange arrows and shade) and a particle–hole symmetric gap of 1.9 meV (Δ_{2D}, dashed blue lines in **g** beyond the bulk superconducting gap (Δ_{bulk}, dashed black lines in **g**) at the 2 × 2 Cs ordered surface. V_{set} = 100 mV, I_t = 3 nA, V_{mod} = 0.1 mV.

wave (PDW) order[2,30], pseudogap behaviour[2] and charge-6e superconductivity in thin-film ring structures[31]. Whether these unconventional quantum phases and the particular interplay between CDW and superconductivity[32,33] can be manipulated and controlled by atomic-scale modifications remains to be shown.

In this work, we investigate the emergent quantum states and their atomic manipulation in AV_3Sb_5. We unveil the emergence of a particle–hole symmetric energy gap at the Cs reconstructed surface of CsV_3Sb_5 via low-temperature scanning tunnelling microscopy/spectroscopy (STM/STS). We systematically study the temperature dependence and magnetic field evolution, image the magnetic vortex states and identify the energy gap as an emergent quasi-2D superconducting state from the band of bound states localized near the surface with stacking dislocations. This 2D superconductivity is distinct from the bulk superconducting state and has significantly higher critical temperature ($T_c \approx$ 5.4 K), higher out-of-plane critical magnetic field ($H_{c2} \approx$ 8 T) and a larger two-gap to T_c ratio (~7.3) than those associated with the bulk superconductivity in CsV_3Sb_5. This superconducting state exhibits unconventional vortex core excitations and 4 × 4 spatial modulations of the superconducting coherence peak and the superconducting gap size, consistent with a 3Q primary PDW. Moreover, we demonstrate that this quasi-2D superconducting state can be controlled at the atomic level. By manipulating the surface Cs atoms to create or eliminate π-phase dislocations in the bulk CDW, we toggle the quasi-2D superconductivity on and off, hence manipulating the quantum phases through atomic engineering.

We propose a mechanism for the emergence of a distinct superconducting state, induced by a Cs-adatoms-driven phase twist at the stacking surface of bulk CDW orders, as shown schematically (Fig. 1b,c). The CDW state in AV_3Sb_5 is three-dimensional (3D) with strong interlayer correlations. It can be thought of as a phase coherent stacking along the c-axis of $2a_0 \times 2a_0$ (2 × 2 in short) charge density modulations in the kagome plane. The stabilized 2 × 2 × 2 order at low temperatures creates a bulk CDW energy gap in the electronic density of states (Fig. 1b). If the 2 × 2 ordered Cs atoms can be formed and atomically tuned out of phase with the bulk CDW, a π-phase-shift dislocation stacking fault is introduced on the surface, leading to a quasi-2D surface band and superconducting gap (Fig. 1c).

The 2 × 2 ordered Cs surface and emergent energy gap

The CsV_3Sb_5 single crystals are cleaved at low temperature (see the Methods for details). Apart from the well-known Cs reconstructions on cleaved surfaces reported previously (Supplementary Fig. 1), we observe a new type of ordered Cs structure in some surface regions (Fig. 1d and Supplementary Fig. 3). The STM topographic image and its

Fourier transform (FT) reveal a hexagonal lattice with the periodicity of about 1.1 nm, twice that of the crystalline lattice constant a_0, demonstrating the 2 × 2 ordered superlattice structure (Fig. 1d). To further reveal the atomic configuration of Cs atoms, we intentionally push some of them away by STM tip to expose a small area of the Sb2 surface below[2] (Fig. 1e). We identify that each Cs atom in the 2 × 2 superstructure is located right above the centre of the Sb2 honeycomb lattice, which is directly above the Sb1 atom at the centre of the hexagons in the V kagome lattice (Fig. 1a). Observations of 2 × 2 Cs superstructures are reproducible on all samples cleaved at low temperature. The largest area of 2 × 2 Cs ordered surface is about 150 nm × 150 nm (see the Methods for details).

In sharp contrast to other types of surfaces such as √3 × √3 ordered or the Sb2 surface, where the spectra show a density of states suppression over a broad soft CDW energy gap, a series of narrow bands of bound states emerge inside the bulk CDW gap on the 2 × 2 ordered Cs surfaces, with the sharpest spectral peak located at about 5.6 mV (P_{2D}) above the Fermi level (E_F; Fig. 1f). The full width at half maximum of the peak is about 2 mV, and its intensity is nearly five times larger than the background tunnelling conductance from the bulk bands (Fig. 1f,g). These incipient bands of near mid-gap states are unexpected, as the 2 × 2 ordered Cs atoms have the same planar periodicity as the bulk 2 × 2 × 2 CDW order, indicating their intricate interplay, which we will discuss further below.

The tunnelling conductance at low energies shows a significantly enhanced density of states near the E_F, elevated by the tail end of the in-gap states peaked at P_{2D}, exclusively on the 2 × 2 ordered Cs surfaces (Fig. 1f). Intriguingly, a new pair of conductance peaks develops at around ±1.9 mV, delineating an emergent particle–hole symmetric gap labelled as Δ_{2D} (Fig. 1g). From hundreds of dI/dV spectra collected over different 2 × 2 Cs ordered regions of six CsV_3Sb_5 samples, we obtain an average gap size of $\Delta_{2D} \approx 1.70 \pm 0.17$ meV (Extended Data Fig. 1a). This is in sharp contrast to other types of surfaces, where only the bulk superconducting gap $\Delta_{bulk} \approx 0.5$ meV was observed below $T_{c,bulk} \approx 2.5$ K that is present as a distinct in-gap feature inside Δ_{2D} on the newly-discovered 2 × 2 Cs ordered surfaces (Fig. 1g). The dI/dV maps covering the boundary between 2 × 2 Cs ordered region and other types of Cs reconstructions show that the dominant intensity at 2 and 5 mV are localized in the 2 × 2 Cs ordered region, whereas no difference is observed across the boundary at zero energy (Extended Data Fig. 1b–e). These observations further demonstrate that the Δ_{2D} and P_{2D} emerge from and are characteristic of the quasi-2D surface states on the 2 × 2 Cs ordered surfaces.

A new quasi-2D superconducting state and 4 × 4 PDW

Applying external magnetic fields perpendicular to the sample surfaces, we observe that the bulk superconducting gap Δ_{bulk} is fully suppressed above the upper critical field $H_{c2,bulk} \approx 0.8$ T (ref. 34) (Fig. 2a), while Δ_{2D} survives and becomes undetectable only at a much larger critical field of $H_{c2,2D} \approx 8.0$ T. In addition, the suppression of Δ_{2D} is independent of the perpendicular field direction (Fig. 2b), excluding the possibility of local magnetic states (for example, spin singlet states[35]) in 2 × 2 Cs ordered regions for the non-magnetic CsV_3Sb_5 crystal. Next, increasing temperature in the absence of an external magnetic field, the bulk superconducting gap Δ_{bulk} closes and is undetectable above a critical temperature of $T_{c,bulk} \approx 2.3$ K (ref. 2), whereas the quasi-2D energy gap Δ_{2D} persists up to $T_{c,2D} \approx 5.4$ K (Fig. 2c,d). The peak-to-peak gap value of Δ_{2D} (Fig. 2e) exhibits a similar temperature dependence to the bulk superconducting gap Δ_{bulk} (ref. 36). Thus, the field- and temperature-dependent measurements suggest that Δ_{2D} most probably originates from an intrinsic quasi-2D superconductivity rather than a proximity-effect-induced superconductivity. The value of the measured gap-to-T_c ratio $2\Delta_{2D}/k_BT_c \approx 7.3$ is significantly larger than that of bulk superconductivity (~5.2) (ref. 2). We attribute this new superconducting state as quasi-2D superconducting state since it is detectable only on the 2D 2 × 2 Cs reconstruction surfaces, and lack of further evidence for a complete 2D origin, such as Berezinskii–Kosterlitz–Thouless transition, due to instrument constraints.

The superconductivity origin of Δ_{2D} is further confirmed by the observation of Abrikosov vortices (Fig. 2f–i) in a perpendicular magnetic field B_z. At 0.4 K and B_z = 0 T, the zero-bias conductance map is essentially uniform (Fig. 2g and Supplementary Fig. 7). When B_z is well above the bulk $H_{c2,bulk} \approx 0.8$ T, Δ_{bulk} is fully suppressed and the vortex lattice of the bulk superconducting state is undetectable[37] (Supplementary Fig. 8). However, several bound-state cores with high spectral intensity labelled as V1, V2 and V3 (Fig. 2h) are observed at 1.5 T in the zero-bias conductance map of the 2 × 2 Cs ordered region where Δ_{2D} is present. The comparison between the zero-bias conductance map at 0 T and 1.5 T of the same surface region rules out the local impurity-induced bound states as the origin. When B_z is increased to 1.7 T, the core positions change with the field (marked V1′ and V2′ in Fig. 2i). The distance between two neighbouring vortex cores decreases from 40 nm at 1.5 T to about 21 nm at 3.5 T (Supplementary Fig. 9), demonstrating the formation of the Abrikosov vortex lattice[37]. In addition, the dI/dV linecut across the core shows the emergence of vortex bound states inside Δ_{2D} (Fig. 2j,k). These observations demonstrate the existence of field-induced vortex lattice arising from the quasi-2D superconductivity associated with the energy gap Δ_{2D}. A rough estimate of the vortex core size gives a coherence length of 6–8 nm, which is about three times smaller than the coherence length of the bulk superconducting state derived from bulk vortex core size ~26 nm (ref. 38) (Supplementary Fig. 10). Since the critical field scales with the inverse of the coherence length squared, we arrive at a critical field that is about ten times larger than that of the bulk superconducting states, which is indeed consistent with our observation of $H_{c2,2D} \approx 8$ T discussed above. We note that the vortex bound states exhibit a plateau-like density of states around zero energy (Fig. 2j), which is distinct from the conventional Caroli–de Gennes–Matricon states observed in bulk superconducting state of CsV_3Sb_5 (ref. 37) (Supplementary Fig. 11).

The emergent quasi-2D superconductivity may harbour intertwined quantum states invisible in the 3D compounds. We have thus studied the spatial distribution of the superconducting properties and observed the emergence of a 4 × 4 spatial modulation, which is twice the periodicity of the 2 × 2 Cs order, directly visible in the dI/dV maps (Fig. 3a, dashed white circle). They give rise to three prominent peaks located at half the length of $\mathbf{Q}_{2\times2}$ in the FT pattern (Fig. 3b, green circles). The new short-range ordered 4 × 4 modulations emerge only at low energies (for example, −1.6 meV) (Fig. 3a) while become undetectable at relatively higher energies (for example, 6.4 meV) (Fig. 3c,d). The FT intensity along one lattice direction (Fig. 3b, dashed red line) as a function of sample bias shows that the modulation wave vector, that is, $\mathbf{Q}_{4\times4}$, does not depend on the bias energy and is non-dispersive (Fig. 3e). In addition, $\mathbf{Q}_{4\times4}$ is observed over the entire energy range of the density of states buildup due to the quasi-2D superconducting coherence (Fig. 3e, right), which is different from the modulations caused by the quasiparticle interference due to impurity scattering that should be limited to the very narrow energy window of the coherence peaks[39]. These observations are reproducible in different 2 × 2 Cs ordered regions of various samples (Supplementary Fig. 13) and support that the 4 × 4 ordered modulations, the first of its kind observed in kagome superconductors, is correlated to and a part of the emergent quasi-2D superconductivity.

To directly test this picture, we further study the spatial variation of the quasi-2D superconducting gap size Δ_{2D} by collecting the dI/dV spectra along a linecut (Fig. 3a, green arrow), which shows sizable variations in the distance between the pair of coherence peaks associated with Δ_{2D} (Fig. 3f). The local gap sizes Δ_{2D} can be more precisely extracted from the peak locations in the $-d^3I/dV^3$ curves as marked by the black crosses (Fig. 3g), which exhibit systematic modulations of only the quasi-2D superconducting gap across the linecut (Supplementary

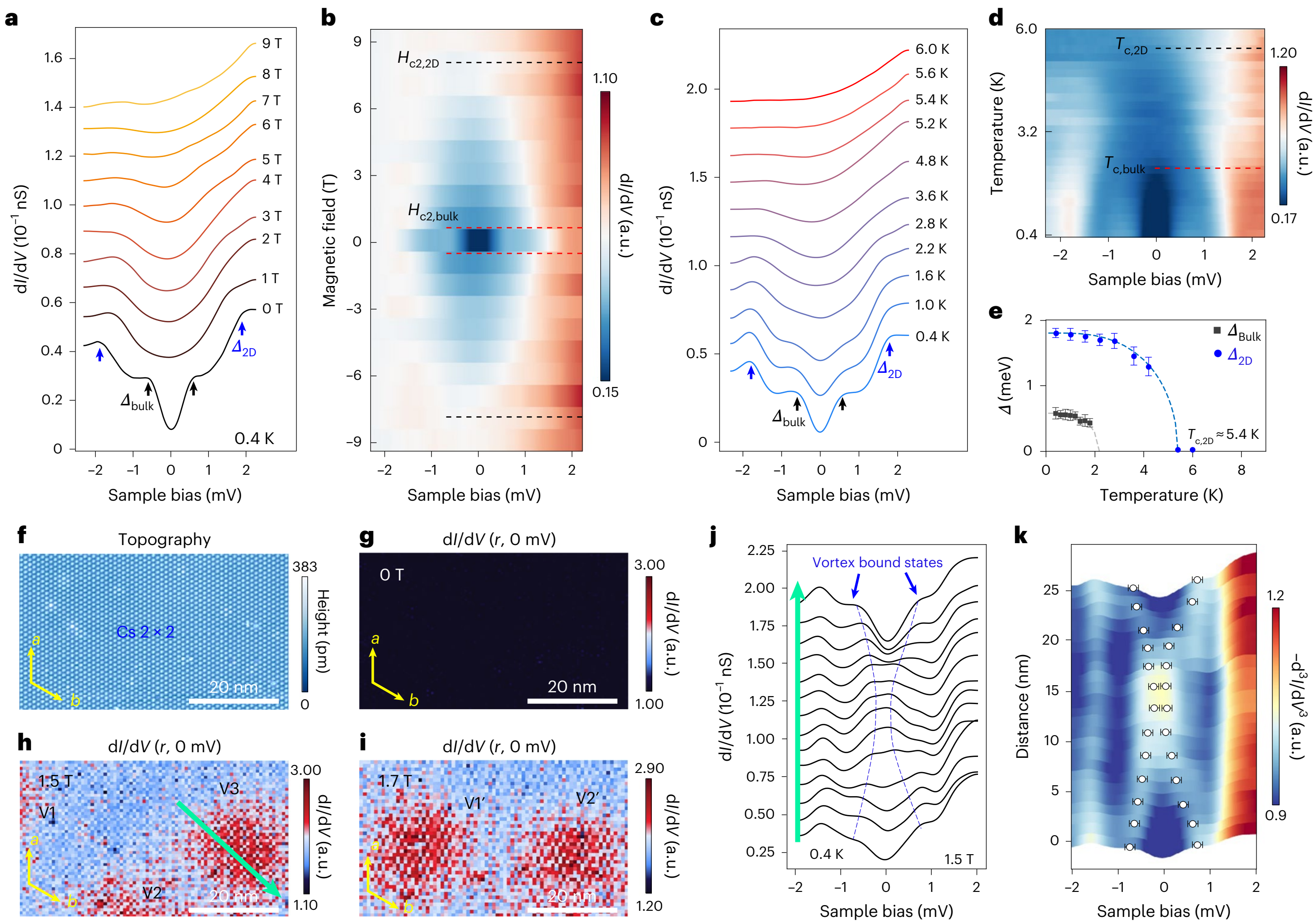

Fig. 2 | Superconductivity origin of Δ_{2D} at the 2 × 2 Cs ordered surface of CsV_3Sb_5. a, The out-of-plane magnetic field dependence of spatially averaged dI/dV spectra (Supplementary Fig. 4), showing the suppression of Δ_{bulk} (black arrows) and Δ_{2D} (blue arrows). **b**, A colour map of dI/dV spectra from −9 to 9 T, showing the magnetic-field-induced suppression of Δ_{2D}, independent of the field direction. The H_{c2} of Δ_{2D} ($H_{c2,2D}$) is about 8 T (black dashed line), which is much higher than the $H_{c2,bulk}$ of Δ_{bulk} (0.8 T, dashed red line). **c**,**d**, The temperature dependence of spatially averaged dI/dV spectra (**c**) and colour map (**d**), showing that the critical temperature of Δ_{2D} ($T_{c,2D}$, dashed black line) is significantly higher than that of bulk superconducting gap ($T_{c,2D}$, dashed red line). More temperature-dependent spectra are shown in Supplementary Fig. 5. **e**, Evolution of Δ_{bulk} and Δ_{2D} with temperature extracted from the dI/dV spectra in **c**, showing the bulk superconductivity with $T_{c,bulk} \approx 2.3$ K and $T_{c,2D} \approx 5.4$ K. The dashed blue curve is the BCS simulation of superconducting gap size evolution. **f**–**i**, An STM topography of a 2 × 2 Cs ordered surface (**f**) (V_{set} = 900 mV, I_t = 50 pA) and corresponding zero-energy dI/dV maps under out-of-plane magnetic field of 0.0 T (**g**), 1.5 T (**h**) and 1.7 T (**i**), respectively, showing field-induced Abrikosov vortex lattice from Δ_{2D}. The vortices in **h** and **i** are labelled as V_1–V_3 and V_1'–V_2', respectively. **j**,**k**, The waterfall plot of dI/dV spectra (**j**) and corresponding intensity plot of the negative third derivative conductance, −d^3I/dV^3 spectra (**h**) along the cyan arrow in **h**, showing the bound states inside Δ_{2D} across the vortex core. For all dI/dV data in this figure, V_{set} = 50 mV, I_t = 2 nA and V_{mod} = 0.1 mV. The spectra in **a**, **c** and **j** are vertically shifted for clarity. The error bars in **e** represent the FWHM obtained by the Gaussian fitted coherence peak (Supplementary Fig. 6) of the spectra shown in **c**. The error bars in **j** represent the energy resolution in STS measurements.

Fig. 14). The spatial modulation of Δ_{2D} has an amplitude of the order of 5.5% of the average gap. Intriguingly, the spatial modulations can be well described by two distinct periods of $2a_0$ and $4a_0$, respectively (Fig. 3g, dashed black curve), corresponding to an intraunit-cell 2 × 2 pair density modulation[40,41] and a primary 4 × 4 PDW within a finite size. We thus attribute both the pair density modulation and the PDW formation to the emergent quasi-2D superconductivity. But as our map size is only a few tens of nanometres, we cannot rule out that the PDW is a short-ranged order with the correlation length of the region size.

Atomic manipulation of quasi-2D superconducting state

To investigate the physical conditions for the emergent quasi-2D superconductivity, we create in situ triangular-shaped 2 × 2 Cs ordered islands with designed configurations by manipulating the Cs adatoms using the STM tip in the same surface region (Fig. 4a, Supplementary Fig. 18 and Methods). Such engineered surface superstructures can avoid the possible spatial inhomogeneity (Supplementary Fig. 17 and Methods) of the as-cleaved surface of CsV_3Sb_5.

The first necessary condition for pronounced superconducting gap Δ_{2D} to appear is the critical size of the 2 × 2 region must be larger than the coherence length of the quasi-2D superconductivity. We define the size of a region by the atom number N on the edge of the isosceles triangle island with 2 × 2 Cs order (Fig. 4b). For small-sized island ($N < 13$), we observe only the bulk superconducting gap Δ_{bulk} appearing below $T_{c,bulk}$ and small peaks around 5 mV arising from the pseudogap phase[2,42] (Fig. 4c and Supplementary Fig. 20). When the island size is increased to $N = 13$, a pronounced peak P_{2D} starts to become observable at 7.8 mV while Δ_{2D} is still undetectable. When the island size is further increased to $N > 19$, Δ_{2D} at around ±1.9 mV begins to be visible (Fig. 4c, dashed red line). The critical size N for emergent Δ_{2D} is approximately 20. Thus, the critical edge length of triangle is about

https://doi.org/10.1038/s41565-025-01940-1

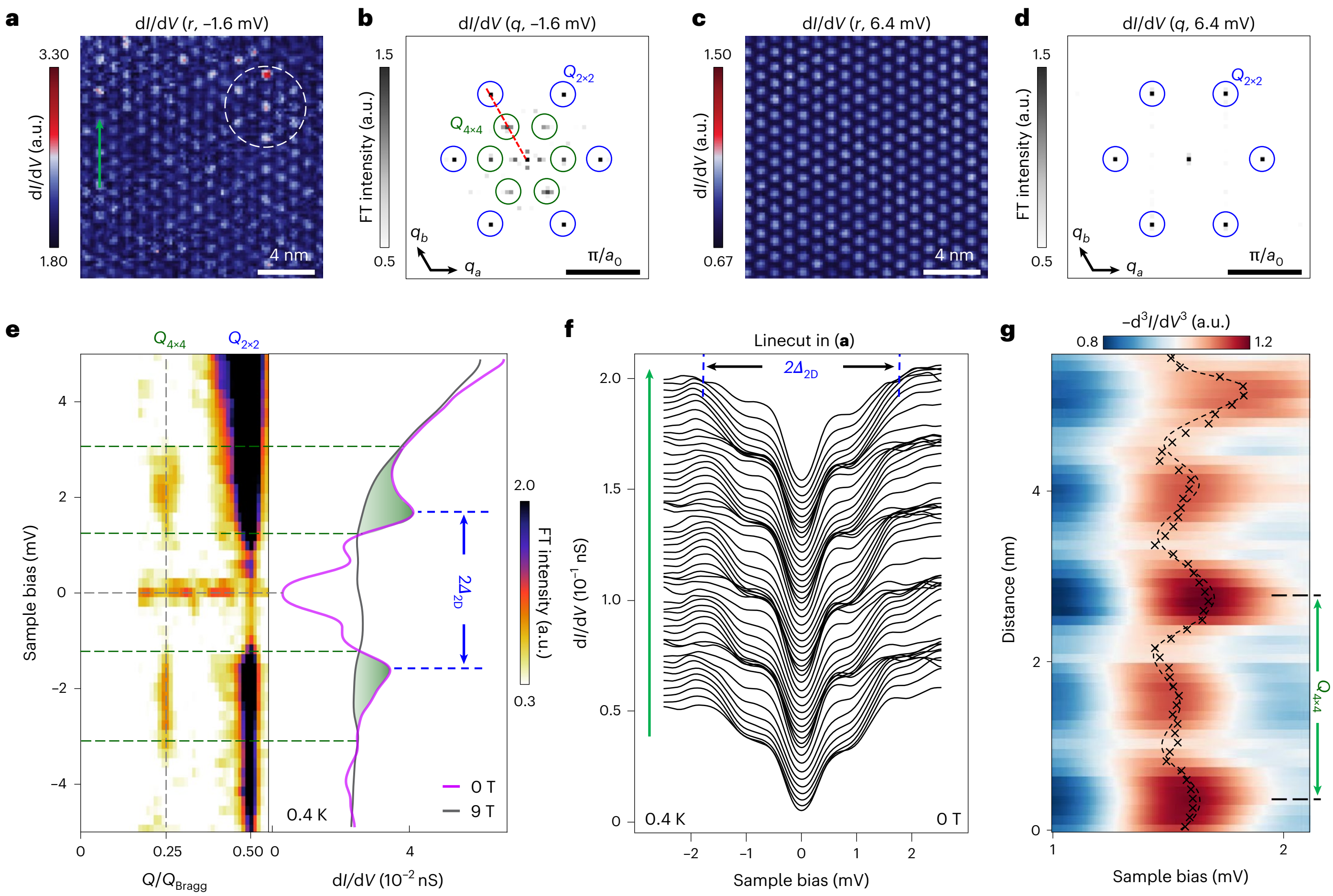

Fig. 3 | Observation of the 4 × 4 PDW modulation of Δ_{2D} at the 2 × 2 Cs ordered surface of CsV_3Sb_5. a,**b**, A d*I*/d*V* map at –1.6 mV (**a**) and the magnitude of the drift-corrected FT (**b**), showing the emergence of short-range ordered 4 × 4 spatial modulation (green circle). For the unprocessed data, see Supplementary Fig. 12. **c**,**d**, A d*I*/d*V* map at 6.4 mV (**c**) and the magnitude of the drift-corrected FT (**d**) in the same region as **a**, showing a uniform 2 × 2 lattice without 4 × 4 superlattice. **e**, Left: an FT linecut of d*I*/d*V* maps along one of three lattice direction (the dashed red line in **b**) at 0.4 K as a function of sample bias, showing that ordering vectors at $\mathbf{Q}_{4\times4}$ is non-dispersive. Right: the energy range of $\mathbf{Q}_{4\times4}$ corresponds to the quasi-2D coherence as indicated by the comparison of d*I*/d*V* spectra between 0 and 9 T. The dashed green lines and green shade are guidelines for the comparison. The dashed blue lines highlight the quasi-2D superconducting gap. The signals near $\mathbf{Q} = 0$ are manually set to 0 for clarity. **f**, The waterfall plot of a d*I*/d*V* linecut along green arrow in **a**, showing spatial modulation of Δ_{2D}. **g**, The zoom-in intensity plot of $-\mathrm{d}^3I/\mathrm{d}V^3$ linecut corresponding to **f**, highlighting that the spatial modulation of Δ_{2D} (black crosses) can be well described by two distinct periods of $2a_0$ and $4a_0$ (dashed black curve), respectively. For all d*I*/d*V* data, $V_{set} = 50$ mV, $I_t = 1.5$ nA, $V_{mod} = 0.15$ mV. The spectra in **f** are vertically shifted for clarity.

20.9 nm. The observed size dependence of P_{2D} and Δ_{2D} is summarized in Fig. 4d. Accordingly, the critical linear dimension of the quasi-2D superconductivity, defined as the distance from centre to the edge of the triangular island, is estimated to be approximately 6 nm, which is indeed comparable with the superconducting coherence length estimated from the size of the vortex core.

The second condition involves the correlation between the superlattice potential of the surface Cs order and the 3D bulk CDW in CsV_3Sb_5. As mentioned above (Fig. 1a), each 2 × 2 unit cell in the surface region contains one Cs atom, which can occupy one of four equivalent sites located above the centres of the four hexagons in the 2 × 2 unit cell of the vanadium kagome lattice below. These four configurations are related by either half a unit-cell translation, that is, a π shift. This $Z_2 \times Z_2$ degeneracy is lifted when the coupling to the bulk CDW is considered. In CsV_3Sb_5, the CDW has the periodicity of 2 × 2 × 2 at low temperatures as determined by STM[38] and scattering experiments[14]. Although the precise nature is still under intensive investigation, where periodicity of 2 × 2 × 4 is also reported[43], it is believed to be a layer stacking of bond ordered CDW with the 2 × 2 star of David (SD) or inverse SD (ISD) configuration in the kagome plane[25,43]. We can therefore label the bulk CDW by a stacking sequence of ABABAB… along the *c* axis, where A and B represent either two ISD (or two SD) configurations with a lateral π shift in one of the three lattice directions or a direct in-phase stacking of ISD and SD configurations. Since the ISD and the SD patterns are centred on one of the four hexagons in the 2 × 2 unit cell in the kagome plane, it is clear that only one of the four 2 × 2 Cs ordered configurations is in-phase with the out-of-plane stacking of the bulk CDW, while the other three interrupt the bulk CDW with a π-phase twist stacking fault at the surface. This three-to-one (3:1) ratio for the π-phase twisted to the in-phase terminations will be the same across all specific realizations of the 2 × 2 × 2 bulk CDW.

As an example, we consider the 2 × 2 × 2 CDW formed by stacking the ISD in the kagome plane with a lateral π shift in the out-of-plane direction[11,44], which is the ground state in density functional theory (DFT) calculations[11]. We extend the DFT analysis to explore how a 2 × 2 Cs ordered surface couples to the bulk CDW (Methods). The results show that the 2 × 2 CDW in the top vanadium kagome plane is always locked to the 2 × 2 Cs order on the surface, such that the centre of the ISD pattern shifts to align directly underneath the occupied Cs site in the 2 × 2 unit cell (Extended Data Fig. 2). This is due to the small binding energy (~10 meV) for the lateral π-phase-shifted stacking of the ISD[11], compared with the large pinning energy due to the Cs atomic order.

https://doi.org/10.1038/s41565-025-01940-1

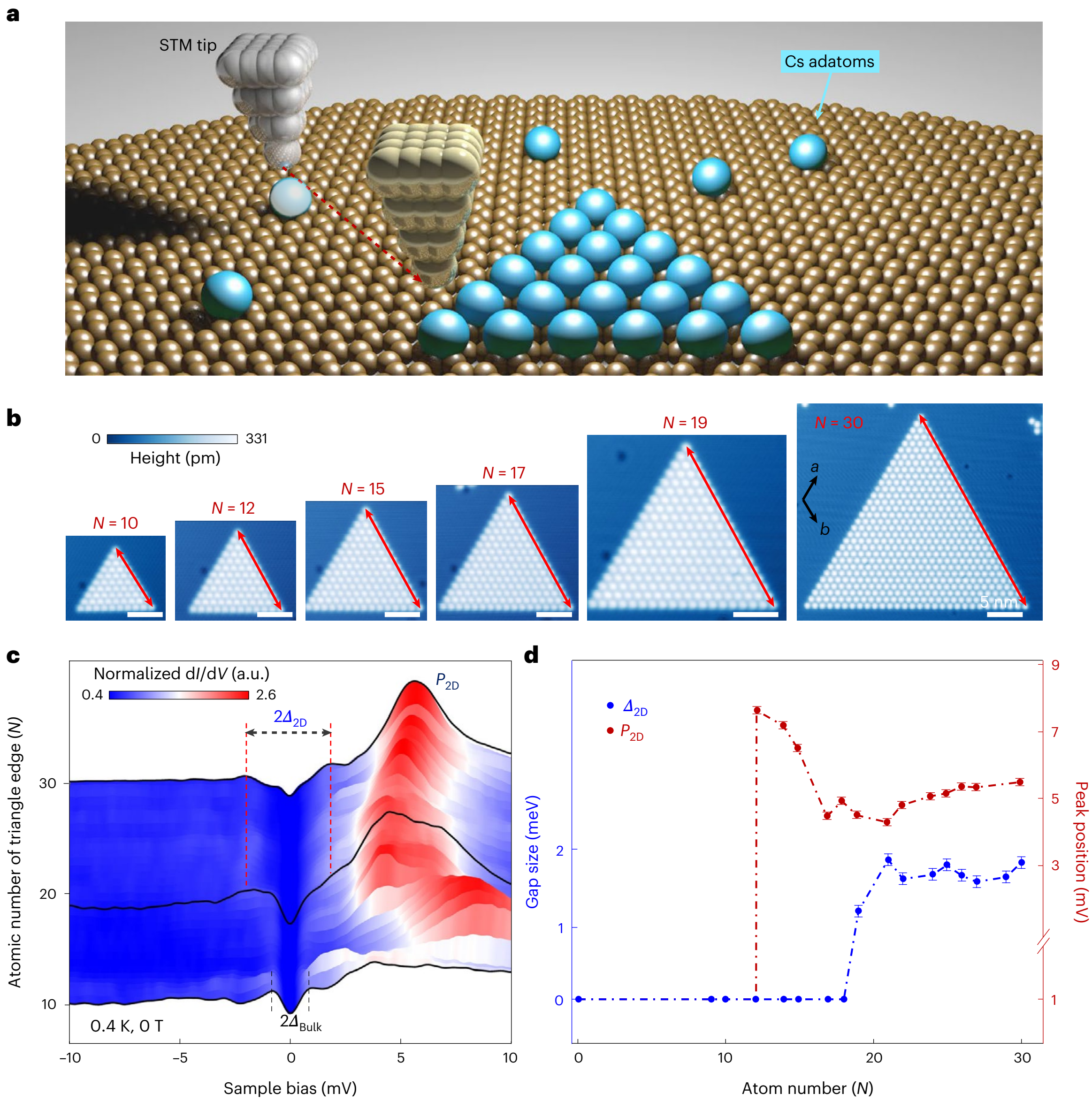

Fig. 4 | Atomic manipulation of quasi-2D superconducting states through artificial control of the size of 2 × 2 Cs ordered region. a, A schematic showing the construction of artificially 2 × 2 reconstructed triangular nano islands by STM manipulation. **b**, Typical STM topographies showing a series of isosceles triangle islands with 2 × 2 Cs order. The size of the islands, defined by the number of atoms on the edge (red arrows), is $N = 10, 12, 15, 17, 25$ and 30, respectively. $V_{set} = 900$ mV, $I_t = 50$ pA. **c**, The dI/dV spectra of triangle islands with increasing atom number N, showing the critical N for the formation of Δ_{2D} (blue arrows) of 20. To minimize the edge-induced quantum confinement effect (Supplementary Fig. 19), we use the dI/dV spectrum at the centre of triangle to characterize the electronic states for each island. The spectra of $N = 1, 19$ and 30 are highlighted by the black curves. The spectrum is normalized with respect to the average value. **d**, The gap size of Δ_{2D} and energy position of P_{2D} as a function of N, extracted from the dI/dV spectra in **c**, which shows an abrupt appearance of Δ_{2D} at $N = 20$ and P_{2D} (~7.8 mV) at $N = 13$. The P_{2D} gradually shifts to a lower energy of ~5.5 mV at $N = 18$. The error bars represent the energy resolution in STS measurements.

As a result, the possible $Z_2 \times Z_2$ Cs ordered configurations amount to four stacking terminations of the 2 × 2 × 2 CDW at the surface (Fig. 5a). Only one of them, labelled as ABAB, is in-phase with the bulk out-of-plane stacking of the ISD, while the other three interrupt the bulk CDW by a π-phase twist stacking fault at the topmost vanadium kagome layer and are labelled as BBAB, CBAB and DBAB (Fig. 5a). We thus expect the emergence of different kinds of surface states with a 3:1 ratio that are localized in the Cs ordered regions. And the situation is the same when considering a 2 × 2 × 4 CDW (Supplementary Fig. 21).

To test this conjecture and gain microscopic insights, we experimentally construct the four different 2 × 2 Cs ordered terminations with the same size ($N = 25$ triangle) by atomic manipulation using the STM tip (Fig. 5b and Supplementary Fig. 23). They are labelled as configurations I–IV and are related by the marked half-unit cell π shift (Fig. 5c). Remarkably, the dI/dV spectra at the centre of each region show that the incipient in-gap density of states peak P_{2D} at 6.0–6.8 mV, and the superconducting gap Δ_{2D} emerges (cyan, green and blue curves) in configurations II, III and IV, while P_{2D} at about 11.2 mV, and a much weaker feature of Δ_{2D} is observed in configuration I (Fig. 5d, red curve). The P_{2D} indeed shows strong localization features around the 2 × 2 ordered Cs atoms in the dI/dV linecuts (Extended Data Fig. 3). Although STM is only sensitive to the top surface layer, the detected ratio of 3:1 supports that configuration I corresponds to the in-phase ABAB termination while the other three correspond to π-phase twisted stacking fault of the bulk CDW at the surface (Fig. 5a). Therefore, the incipient narrow band P_{2D} near E_F is concurrent with Δ_{2D} (Fig. 5d) and the phase-twisted stacking fault of the bulk CDW state at the surface is the key condition for the emergent

 https://doi.org/10.1038/s41565-025-01940-1

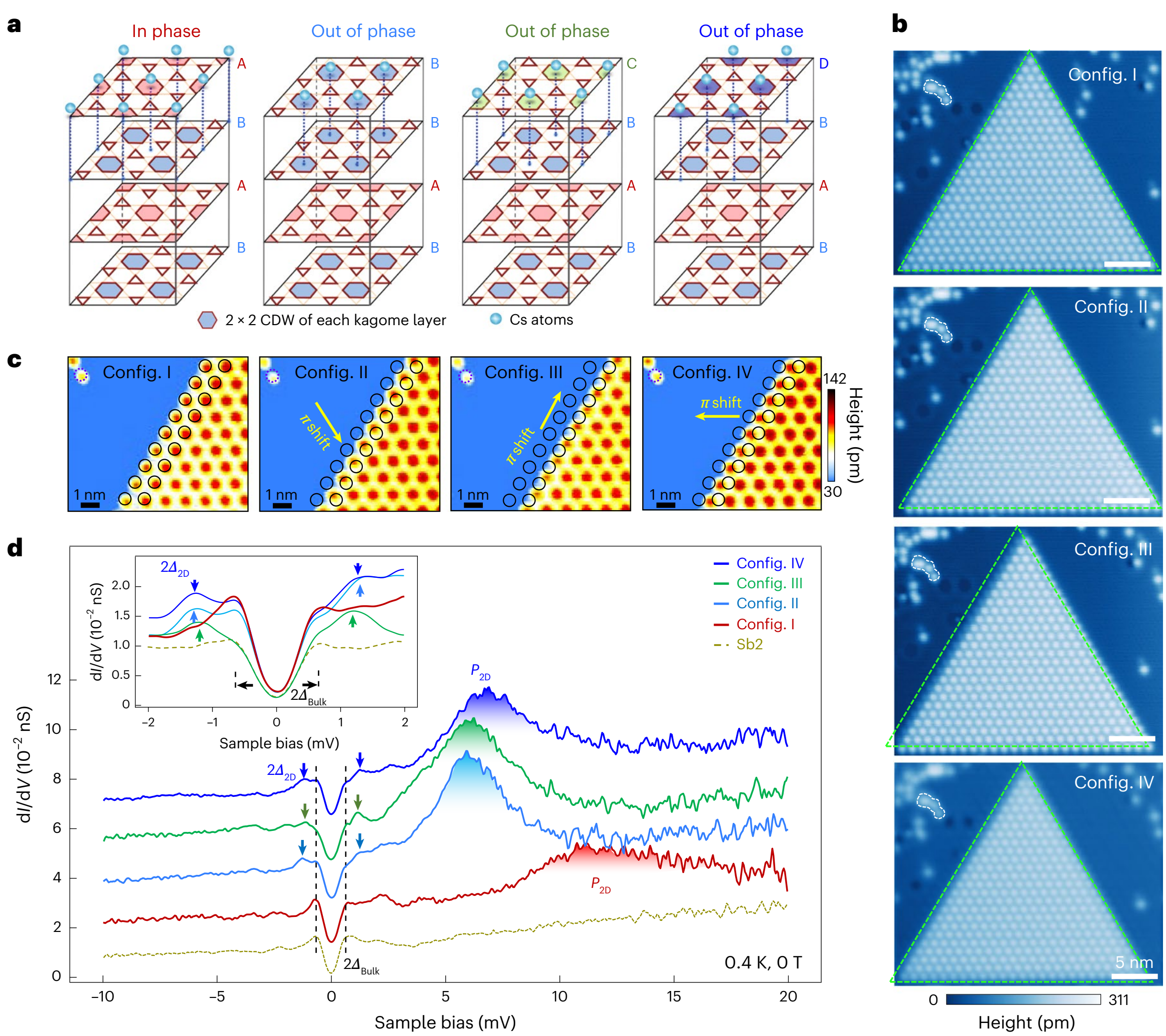

Fig. 5 | Atomic manipulation of the quasi-2D superconducting state through artificial control the phase twist of bulk CDW. a, A schematic of four 2 × 2 Cs ordered surface configurations (config.) by involving the correlation between the superlattice potential of the surface Cs order and 3D bulk CDW. One in-phase configuration fit with the out-of-plane stacking of the bulk CDW, namely ABAB, while the other three out-of-phase configurations disrupt the bulk CDW with a π-phase twist stacking fault at the surface, labelled as BBAB, CBAB and DBAB. **b**, STM topographies showing four different 2 × 2 Cs terminations with the same size, constructed by atomic manipulation using the STM tip in the same surface region. The STM topography for configuration IV is low-pass filtered for clarity (Supplementary Fig. 22). The dashed green triangle marks the position of configuration I in the figure. The dashed white line highlights the marker atoms. Scale bar, 5 nm; V_{set} = 900 mV, I_t = 40 pA. **c**, Zoom-ins of **b**, showing the π-phase shift among four configurations. The colour bar is adjusted to highlight the phase shift. The purple dotted circles highlight the marker atom. The black circles mark the atom position of configuration I in each panel. The yellow arrows show the phase-shift direction of each island respect to the configuration I island. **d**, The d*I*/d*V* spectra at the centre of the four configurations in **b**, respectively, showing that the incipient in-gap density of states peak P_{2D} in one of the four configurations is located at -11.2 mV (red curve), significantly higher than the other three (6.0–6.8 mV). The inset shows a zoom-in of d*I*/d*V* spectra, showing that the feature of emergent Δ_{2D} (coloured arrows) for one configuration (red curve) is much weaker than others. For all d*I*/d*V* data in this figure, V_{set} = 50 mV, I_t = 1.5 nA, V_{mod} = 0.1 mV. The error bars in **c** represent the energy resolution in STS measurements.

quasi-2D superconductivity, which can be switched on and off by atomic manipulation of the Cs atoms.

To further substantiate the correlation between emergent 2D superconductivity and the 3D bulk CDW order (Fig. 1c), we perform additional STM/STS measurements. An important corollary of this mechanism (Methods) is that in the absence of 3D bulk CDW order, 2 × 2 Cs surface reconstruction would be unable to generate the in-gap states on the surface and the quasi-2D superconductivity. To test this, we have grown single crystal of $CsV_{2.85}Ti_{0.15}Sb_5$, where long-range CDW order is suppressed[45] by the significant hole doping due to the Ti substitution of V. The spatially averaged d*I*/d*V* spectra measured on differently reconstructed Cs surfaces, including 2 × 2 Cs ordered regions and the Sb-terminated surface, show no significant differences; both the incipient surface states P_{2D} and the superconducting gap Δ_{2D} are absent (Extended Data Fig. 4). The absence of surface superconducting gap is further supported by the lack of intensity contrast in d*I*/d*V* maps within the range of −2 to 5 mV across the boundaries between 2 × 2 and other types of reconstructions (two exemplary maps are shown in Extended Data Fig. 4). We have also studied single crystals of the other two members of the kagome AV_3Sb_5 family containing different alkali atoms, KV_3Sb_5 and RbV_3Sb_5, which also exhibit 3D bulk CDW order. We have indeed observed the signatures of density of state peak inside the CDW gap and quasi-2D superconducting gap on the 2 × 2 ordered K and Rb surface regions (Extended Data Fig. 5). These observations confirm the robustness and consistency of our findings.

Conclusions

We unveil quasi-2D superconductivity and PDW on artificially engineered 2 × 2 Cs ordered surfaces of kagome metal AV_3Sb_5. We further demonstrate that this quasi-2D superconducting state can be precisely controlled at the atomic level, allowing us to tune the superconductivity on and off by manipulating surface Cs atoms to create or eliminate π-phase dislocations in the bulk CDW. Future microscale reconstruction can potentially be achieved by automated manipulation or chemical method[46], which will enable other experimental techniques such as photoemission spectroscopy or transport to probe CDW metals with artificially controlled CDW phase and their unique physical properties. Our findings provide insights into the interplay between CDW and superconductivity and a method for creation, manipulation and control of quantum many-body states at antiphase boundaries in kagome metals and, potentially, in other quantum materials.

Online content

Any methods, additional references, Nature Portfolio reporting summaries, source data, extended data, supplementary information, acknowledgements, peer review information; details of author contributions and competing interests; and statements of data and code availability are available at https://doi.org/10.1038/s41565-025-01940-1.

References

1. Yang, S. Y. et al. Giant, unconventional anomalous Hall effect in the metallic frustrated magnet candidate, KV_3Sb_5. *Sci. Adv.* **6**, eabb6003 (2020).
2. Chen, H. et al. Roton pair density wave in a strong-coupling kagome superconductor. *Nature* **599**, 222–228 (2021).
3. Guo, C. Y. et al. Switchable chiral transport in charge-ordered kagome metal CsV_3Sb_5. *Nature* **611**, 461–466 (2022).
4. Zhong, Y. G. et al. Nodeless electron pairing in CsV_3Sb_5-derived kagome superconductors. *Nature* **617**, 488–492 (2023).
5. Ortiz, B. R. et al. CsV_3Sb_5: a Z_2 topological kagome metal with a superconducting ground state. *Phys. Rev. Lett.* **125**, 247002 (2020).
6. Ortiz, B. R. et al. New kagome prototype materials: discovery of KV_3Sb_5, RbV_3Sb_5, and CsV_3Sb_5. *Phys. Rev. Mater.* **3**, 094407 (2019).
7. Han, T.-H. et al. Fractionalized excitations in the spin-liquid state of a kagome-lattice antiferromagnet. *Nature* **492**, 406–410 (2012).
8. Yin, J. X. et al. Giant and anisotropic many-body spin-orbit tunability in a strongly spin-orbit tunability in a strongly correlated kagome magnet. *Nature* **562**, 91–95 (2018).
9. Liu, D. F. et al. Magnetic Weyl semimetal phase in a kagomé crystal. *Science* **365**, 1282–1285 (2019).
10. Yin, Q. W. et al. Superconductivity and normal-state properties of kagome metal RbV_3Sb_5 single crystals. *Chin. Phys. Lett.* **38**, 037403 (2021).
11. Tan, H. X. et al. Charge density waves and electronic properties of superconducting kagome metals. *Phys. Rev. Lett.* **127**, 046401 (2021).
12. Xing, Y. et al. Optical manipulation of the charge-density-wave state in RbV_3Sb_5. *Nature* **631**, 60–66 (2024).
13. Kang, M. G. et al. Charge order landscape and competition with superconductivity in kagome metals. *Nat. Mater.* **22**, 186–193 (2023).
14. Li, H. X. et al. Observation of unconventional charge density wave without acoustic phonon anomaly in kagome superconductors AV_3Sb_5 (A = Rb, Cs). *Phys. Rev. X* **11**, 031050 (2021).
15. Xiang, Y. et al. Twofold symmetry of *c*-axis resistivity in topological kagome superconductor CsV_3Sb_5 with in-plane rotating magnetic field. *Nat. Commun.* **12**, 6727 (2021).
16. Zhao, H. et al. Cascade of correlated electron states in the kagome superconductor CsV_3Sb_5. *Nature* **599**, 216–221 (2021).
17. Li, H. et al. Rotation symmetry breaking in the normal state of a kagome superconductor KV_3Sb_5. *Nat. Phys.* **18**, 265–270 (2022).
18. Li, H. et al. Unidirectional coherent quasiparticles in the high-temperature rotational symmetry broken phase of AV_3Sb_5 kagome superconductors. *Nat. Phys.* **19**, 637–643 (2023).
19. Zheng, L. X. et al. Emergent charge order in pressurized kagome superconductor CsV_3Sb_5. *Nature* **611**, 682–687 (2022).
20. Hu, B. et al. Robustness of the unidirectional stripe order in the kagome superconductor CsV_3Sb_5. *Chin. Phys. B* **31**, 058102 (2022).
21. Nie, L. P. et al. Charge-density-wave-driven electronic nematicity in a kagome superconductor. *Nature* **604**, 59–64 (2022).
22. Wu, P. et al. Unidirectional electron-phonon coupling in the nematic state of a kagome superconductor. *Nat. Phys.* **19**, 1143–1149 (2023).
23. Asaba, T. et al. Evidence for an odd-parity nematic phase above the charge-density-wave transition in a kagome metal. *Nat. Phys.* **20**, 40–46 (2024).
24. Mielke, C. et al. Time-reversal symmetry-breaking charge order in a kagome superconductor. *Nature* **602**, 245–250 (2022).
25. Xu, Y. S. et al. Three-state nematicity and magneto-optical Kerr effect in the charge density waves in kagome superconductors. *Nat. Phys.* **18**, 1470–1475 (2022).
26. Jiang, Y. X. et al. Unconventional chiral charge order in kagome superconductor KV_3Sb_5. *Nat. Mater.* **20**, 1353–1357 (2021).
27. Saykin, D. R. et al. High resolution polar kerr effect studies of CsV_3Sb_5: tests for time-reversal symmetry breaking below the charge-order transition. *Phys. Rev. Lett.* **131**, 016901 (2023).
28. Farhang, C. et al. Unconventional specular optical rotation in the charge ordered state of Kagome metal CsV_3Sb_5. *Nat. Commun.* **14**, 5326 (2023).
29. Le, T. et al. Superconducting diode effect and interference patterns in kagome CsV_3Sb_5. *Nature* **630**, 64–69 (2024).
30. Deng, H. et al. Chiral kagome superconductivity modulations with residual Fermi arcs. *Nature* **632**, 775–781 (2024).
31. Ge, J. et al. Charge-4*e* and charge-6*e* flux quantization and higher charge superconductivity in kagome superconductor ring devices. *Phys. Rev. X* **14**, 021025 (2024).
32. Wilson, S. D. & Ortiz, B. R. AV_3Sb_5 kagome superconductors. *Nat. Rev. Mater.* **9**, 420–432 (2024).
33. Guo, C. Y. et al. Correlated order at the tipping point in the kagome metal CsV_3Sb_5. *Nat. Phys.* **20**, 579–584 (2024).
34. Ni, S. L. et al. Anisotropic superconducting properties of kagome metal CsV_3Sb_5. *Chin. Phys. Lett.* **38**, 057403 (2021).
35. Li, W. et al. Phase separation and magnetic order in K-doped iron selenide superconductor. *Nat. Phys.* **8**, 126–130 (2012).
36. Machida, T. et al. A scanning tunneling microscope for spectroscopic imaging below 90 mK in magnetic fields up to 17.5 T. *Rev. Sci. Instrum.* **89**, 093707 (2018).
37. Huang, Z. H. et al. Tunable vortex bound states in multiband CsV_3Sb_5-derived kagome superconductors. *Sci. Bull.* **69**, 885–892 (2024).
38. Liang, Z. et al. Three-dimensional charge density wave and surface-dependent vortex-core states in a kagome superconductor CsV_3Sb_5. *Phys. Rev. X* **11**, 031026 (2021).
39. Gao, Z. Q. et al. Pair-breaking scattering interference as a mechanism for superconducting gap modulation. *Phys. Rev. B* **110**, 224509 (2024).
40. Wei, T. H. et al. Observation of superconducting pair density modulation within lattice unit cell. *Chin. Phys. Lett.* **42**, 027404 (2025).
41. Kong, L. Y. et al. Cooper-pair density modulation state in an iron-based superconductor. *Nature* **640**, 55–61 (2025).
42. Zhou, S. & Wang, Z. Chern Fermi pocket, topological pair density wave, and charge-4*e* and charge-6*e* superconductivity in kagomé superconductors. *Nat. Commun.* **13**, 7288 (2022).
43. Ortiz, B. R. et al. Fermi surface mapping and the nature of charge-density-wave order in the kagome superconductor CsV_3Sb_5. *Phys. Rev. X* **11**, 041030 (2021).
44. Christensen, M. H. et al. Theory of the charge density wave in AV_3Sb_5 kagome metals. *Phys. Rev. B* **104**, 214513 (2021).

https://doi.org/10.1038/s41565-025-01940-1

45. Yang, H. T. et al. Titanium doped kagome superconductor $CsV_{3-x}Ti_xSb_5$ and two distinct phases. *Sci. Bull.* **67**, 2176–2185 (2022).
46. Mantravadi, A. et al. When van der Waals met kagome: a 2D antimonide with a vanadium–kagome network. *J. Am. Chem. Soc.* **146**, 26786–26800 (2024).

https://doi.org/10.1038/s41565-025-01940-1

Methods

Single crystal growth of pristine Ti-doped CsV_3Sb_5 sample

Single crystals of pristine and Ti-doped CsV_3Sb_5, KV_3Sb_5 and RbV_3Sb_5 were grown via a modified self-flux method.

Formation of large-scale 2 × 2 alkali ordered surface

The 2 × 2 Cs ordered surfaces were obtained by cleaving CsV_3Sb_5 and Ti-doped CsV_3Sb_5 at low temperature. In CsV_3Sb_5, where the layer kagome V3Sb lattices are sandwiched by two honeycomb Sb2 layers, the weak bonding between Cs layer and neighbouring Sb2 layers results in two types of terminated surfaces, that is, Cs-terminated surfaces and Sb-terminated surfaces. To obtain fresh and clean surfaces for STM measurements, the crystal is cleaved in situ in the ultrahigh vacuum chamber and immediately transferred to the low-temperature STM chamber. The alkali atoms have been proven to be easily diffuse over the surfaces, which results in various alkali surfaces such as full coverage of alkali surfaces (1 × 1) (refs. 16,26,38) and half Cs (ref. 38), √3 × √3R30° (short for R3)[2,47] reconstruction (Supplementary Fig. 1). After cleaving at a temperature ranging from 80 to 100 K, we observed a new 2 × 2 Cs reconstruction. We have cleaved more than ten CsV_3Sb_5 crystals, 2 × 2 Cs reconstructions with various sizes are observed in all samples. Large-area 2 × 2 Cs ordered surfaces are observed in six CsV_3Sb_5 crystals, which have relatively large crystal size (40 mm × 40 mm) and bright appearance by eye (sample $1^\#$–$6^\#$ in Supplementary Fig. 3). The largest area of 2 × 2 Cs reconstruction is about 150 nm × 150 nm. In addition, the formation of 2 × 2 reconstruction is not limited to CsV_3Sb_5 but extended to chemically doped CsV_3Sb_5 crystals (Extended Data Fig. 4) and the whole AV_3Sb_5 (A = K, Rb or Cs) family by cleaving at a low temperature ranging from 80 to 100 K (Extended Data Fig. 5).

STM/STS experiments

The samples used in the STM/STS experiments were immediately transferred to an STM chamber and cooled down to 4.2 K after cleaving at low temperature. Experiments were performed in an ultrahigh vacuum (1×10^{-10} mbar) ultralow temperature STM system equipped with an 11 T magnetic field. All the scanning parameters (setpoint voltage and current) of the STM topographic images are listed in the figure captions. Unless otherwise noted, the STM/STS were obtained at a base temperature of 0.4 K and an electronic temperature of 650 mK, calibrated using a standard superconductor, Nb crystal. The dI/dV spectra were acquired by a standard lock-in amplifier at a modulation frequency of 973.1 Hz. To reduce noise, the dI/dV spectra are softly smoothed via a Gaussian filter. We apply the Lawler–Fujita drift-correction algorithm[48] to the data in Fig. 3 to align the atomic Bragg peaks onto single pixels with coordinates that are even integers. Non-superconducting tungsten tips were fabricated via electrochemical etching and calibrated on a clean Au(111) surface prepared by repeated cycles of sputtering with argon ions and annealing at 500 °C.

DFT calculations

The electronic structures of CsV_3Sb_5 were determined using the DFT, as implemented in the Vienna Ab initio Simulation Package[49]. The calculations for electron-electron exchange interactions relied on the generalized gradient approximation, as parameterized by Perdew–Burke–Ernzerhof[50]. We utilized the inverse SD-type CDW structure[11] for the bulk phase. We performed slab model calculations for surface states using slabs that were four-unit-cells thick. Within these models, the atom positions in the one-unit-cell thickness subsurface layer were fully relaxed until the forces acting on them were reduced to 5 meV Å^{-1}. The plane wave basis was set with an energy cutoff of 300 eV, and the Brillouin zone of the slabs was sampled using a 6 × 6 × 1 k-mesh. To calculate the density of states, we employed the tetrahedron method with Blöchl corrections. The surface band structures and density of states were derived by projecting the slab band structures and density of states onto the atoms within the surface unit cell. Spin-orbit coupling is not considered. By using DFT calculations, we find that the newly formed 2 × 2 ordered surfaces show distinct electronic properties with Sb surface, 1 × 1 and other Cs surfaces (Supplementary Fig. 2).

Discussions of $4/3a_0 \times 4/3a_0$ PDW in bulk superconducting state and $4a_0 \times 4a_0$ PDW in quasi-2D superconducting state

It is instructive to compare the 3**Q** PDW with $4/3a_0 \times 4/3a_0$ and $2a_0 \times 2a_0$ spatial modulations previously observed[2,30] in CsV_3Sb_5. Both $\mathbf{Q}_{4\times4}$ and $\mathbf{Q}_{4/3\times4/3}$ have been predicted theoretically for possible emergent density waves based on the near nesting of the Chern Fermi pockets in the 2 × 2 CDW state on the kagome lattice[42]. There are two main differences between the $\mathbf{Q}_{4\times4}$ and the $\mathbf{Q}_{4/3\times4/3}$, $\mathbf{Q}_{2\times2}$ PDW formation. First, the $\mathbf{Q}_{4\times4}$ PDW is observed in the 2 × 2 Cs ordered regions and is born out of the quasi-2D superconducting state on the surface. The $\mathbf{Q}_{4/3\times4/3}$ and $\mathbf{Q}_{2\times2}$ PDW, on the other hand, is a part of the bulk superconducting state observed on Sb surfaces after pushing the Cs atoms away using the STM tip. Second, the $\mathbf{Q}_{4\times4}$ PDW exists outside the bulk superconducting gap and hovers over the entire energy range of the spectral buildup caused by the quasi-2D superconducting coherence (Fig. 3e), whereas the $\mathbf{Q}_{4/3\times4/3}$ PDW exists over a large energy region defined by a pseudogap much larger than the bulk superconducting gap[2]. While the mechanism for the difference between the bulk[42] and surface PDW is currently lacking, we note that these two PDW wave vectors, $\mathbf{Q}_{4/3\times4/3}$ and $\mathbf{Q}_{4\times4}$, are the same up to the reciprocal lattice wave vectors ($\mathbf{Q}_{4\times4} = \mathbf{Q}_{\mathrm{Bragg}} - \mathbf{Q}_{4/3\times4/3}$). In addition, we stress that the new 3**Q** PDW with 4 × 4 modulations in Cs reconstruction below $T_{c,2D}$ of 5.4 K (Supplementary Fig. 15) is unrelated to the unidirectional (1**Q**) $4a_0$ charge stripe order, which is only observed on the bare Sb-terminated surfaces (Supplementary Fig. 16) over a large energy range below ~60 K (refs. 16,20).

Discussions of the mechanism for the emergent quasi-2D superconducting state

The 2 × 2 Cs order behaves as an out-of-phase surface termination of the 2 × 2 × 2 bulk CDW, creating a narrow band of surface states inside the bulk CDW gap. The significantly enhanced density of states close to the Fermi level enabled the first observation of a stronger superconductivity in the 2D limit of a kagome plane with the observed striking properties. Although the as-cleaved 2 × 2 Cs surface reconstruction enabled our discovery and the atomic engineering of the Cs atoms allowed us to probe the mechanism, the underlying physics we revealed is much more general, and its realizations are not limited to Cs surface reconstruction. For example, emergent electronic states can be created and manipulated using a 2 × 2 superlattice potential and extended beyond the Cs surfaces. The π-phase dislocations can also occur in layered CDW state in the bulk at the stacking faults along the c axis and influence the physical properties. Moreover, given the theoretical predictions for the bulk CDW state to be topological, either in the presence of time-reversal symmetry[5,11], or when time-reversal symmetry is broken[42], it is conceivable that the surface states of the bulk CDW order and the emergent 2D superconductivity have intricate topological properties responsible for the observed unconventional vortex core spectrum.

Spatial inhomogeneity of quasi-2D superconductivity

STM/STS measurements across the sample surface show that not all the 2 × 2 Cs ordered regions exhibit an incipient band of bound states with the P_{2D} close to the E_F and a pronounced superconducting gap Δ_{2D}. The emergence of Δ_{2D} is sensitive to the size of 2 × 2 Cs ordered region. In small-sized areas, Δ_{2D} is undetectable. In addition, even in large-sized surface area, Δ_{2D} is occasionally much weaker than in other areas (Supplementary Fig. 17).

Four configurations of 2 × 2 Cs reconstruction

If solely considering the top unit cell of CsV_3Sb_5, the 2 × 2 configuration DFT calculations demonstrate that the Cs atoms in the top Cs surface play a significant role in the 2 × 2 CDW of underlying kagome layer of first unit cell. The 2 × 2 CDW in the kagome V lattice of top layer is locked by the configurations of 2 × 2 reconstruction. If the Cs in the 2 × 2 reconstruction, at the initial state, is not corresponding to the central hexagonal site of the ISD pattern in the underlying kagome layer, the ISD pattern will eventually shift to fit 2 × 2 reconstruction in the upper Cs layer after surface relaxation while the stacking of CDWs among other underlying kagome layers remain unchanged (Extended Data Fig. 2). Therefore, the 2 × 2 Cs reconstruction, which is strongly locked with the 2 × 2 CDW in the first kagome layer of CsV_3Sb_5, modify the phase termination of bulk 2 × 2 × 2 CDW[38] at the surface, resulting in four configurations of 2 × 2 surface reconstructions (Fig. 5b).

Construction of 2 × 2 Cs ordered triangular nanoislands

The 2 × 2 Cs ordered triangular nanoislands at the Sb surface of CsV_3Sb_5 were constructed by STM manipulation technique, as illustrated by the cartoon in Fig. 4a (created using the software package Blender[51]). A typical manipulation parameter is V_{set} = 5 mV, I_{set} = 300 pA.

We place the probe tip sufficiently far from the sample when imaging so that the interaction between sample and tip does not initiate atomic movement. To move a Cs atom, we let the tip closer to the Cs atom by adjusting the tunnelling junction resistance. The resistance is set by ratio of the tunnelling voltage *V* to the tunnelling current *I*. A sufficiently small resistance results in the strong tip-sample interaction. Such interaction creates a highly localized potential[52] well that traps the Cs adatom under the tip.

We did the manipulation as the following steps:

(1) Move the tip onto the top of a target Cs atom in the Sb surface region with dilute Cs adatoms.
(2) Trap the Cs atom by decreasing resistance.
(3) Move the tip laterally while maintaining *I* constant; The current/z evolution is traced to confirm the movement of the target Cs atom (Supplementary Fig. 24).
(4) Release the adatom at the destination by reverting to the value of resistance used in normal imaging.

The formation of the Cs 2 × 2 ordered nanoisland is achieved by step-by-step manipulation of Cs adatoms toward the designed spatial 2 × 2 positions respective to the lattice of Sb surface by using the method above (Supplementary Fig. 25 and Supplementary Video). We keep the shape of islands as equilateral triangles to rule out the shape effect. Through step-by-step manipulation, the Cs reconstruction with artificial designed triangular shape was constructed. For the four structural configurations of the 2 × 2 reconstruction with exact same size (N = 25 triangle) in Fig. 5b, we firstly constructed one configuration at a Sb surface region with diluted Cs adatoms by the STM manipulation technique as described above. Subsequently, we moved each Cs atom in the as-constructed triangular nanoisland by a distance of one lattice constant (a_0) along one of the three equivalent lattice directions (π-phase shift). As a result, the new configuration with exact same size is constructed at the same surface region (Supplementary Fig. 23).

Data availability

The data that support the plots within this paper are available via Figshare at https://doi.org/10.6084/m9.figshare.28723703 (ref. 53). Other data and information are available from the corresponding authors upon reasonable request.

References

47. Yu, J. et al. Evolution of electronic structure in pristine and Rb-reconstructed surfaces of kagome metal RbV_3Sb_5. *Nano Lett.* **22**, 918–925 (2022).
48. Lawler, M. J. et al. Intra-unit-cell electronic nematicity of the high-T_c copper-oxide pseudogap states. *Nature* **466**, 347–351 (2010).
49. Kresse, G. & Furthmuller, J. Efficient iterative schemes for ab initio total-energy calculations using a plane-wave basis set. *Phys. Rev. B* **54**, 11169–11186 (1996).
50. Perdew, J. P. et al. Generalized gradient approximation made simple. *Phys. Rev. Lett.* **77**, 3865–3868 (1996).
51. Community, B. O. B. 4.4. Blender online community. *blender* https://www.blender.org/ (2025).
52. Stroscio, J. A. & Celotta, R. J. Controlling the dynamics of a single atom in lateral atom manipulation. *Science* **306**, 242–247 (2004).
53. Han, X. H. et al. Raw data underlying the pulication 'Atomic manipulation of the emergent quasi-2D superconductivity and pair density wave in a kagome metal'. *Figshare* https://doi.org/10.6084/m9.figshare.28723703 (2025).

Acknowledgements

The work is supported by grants from the National Natural Science Foundation of China (grant no. 62488201), the National Key Research and Development Projects of China (grant nos. 2022YFA1204100 and 2019YFA0308500), the CAS Project for Young Scientists in Basic Research (grant no. YSBR-003) and the Innovation Program of Quantum Science and Technology (grant no. 2021ZD0302700). B.Y. acknowledges the financial support by the Israel Science Foundation (grant nos. 2932/21 and 2974/23), German Research Foundation (DFG, CRC-183, A02) and by a research grant from the Estate of Gerald Alexander. Z.W. is supported by the US DOE, Basic Energy Sciences (grant no. DE-FG02-99ER45747) and by Research Corporation for Science Advancement (Cottrell SEED award no. 27856).

Author contributions

H.-J.G. and H.C. designed the experiments. X.H., H.C., Z.C., Z.H. and Y.Y. performed the STM/STS experiments and data analysis with technical assistance from C.S. Z.Z. and H.Y. prepared the CsV_3Sb_5 samples. H.T. and B.Y. did the DFT calculations. Z.W. did the theoretical consideration. X.H., H.C., Z.W. and H.-J.G. wrote the manuscript with input from all other authors. H.-J.G. supervised the project.

Competing interests

The authors declare no competing interests.

Additional information

Extended data are available for this paper at https://doi.org/10.1038/s41565-025-01940-1.

Supplementary information The online version contains supplementary material available at https://doi.org/10.1038/s41565-025-01940-1.

Correspondence and requests for materials should be addressed to Hui Chen, Ziqiang Wang or Hong-Jun Gao.

Peer review information *Nature Nanotechnology* thanks the anonymous reviewers for their contribution to the peer review of this work.

 https://doi.org/10.1038/s41565-025-01940-1

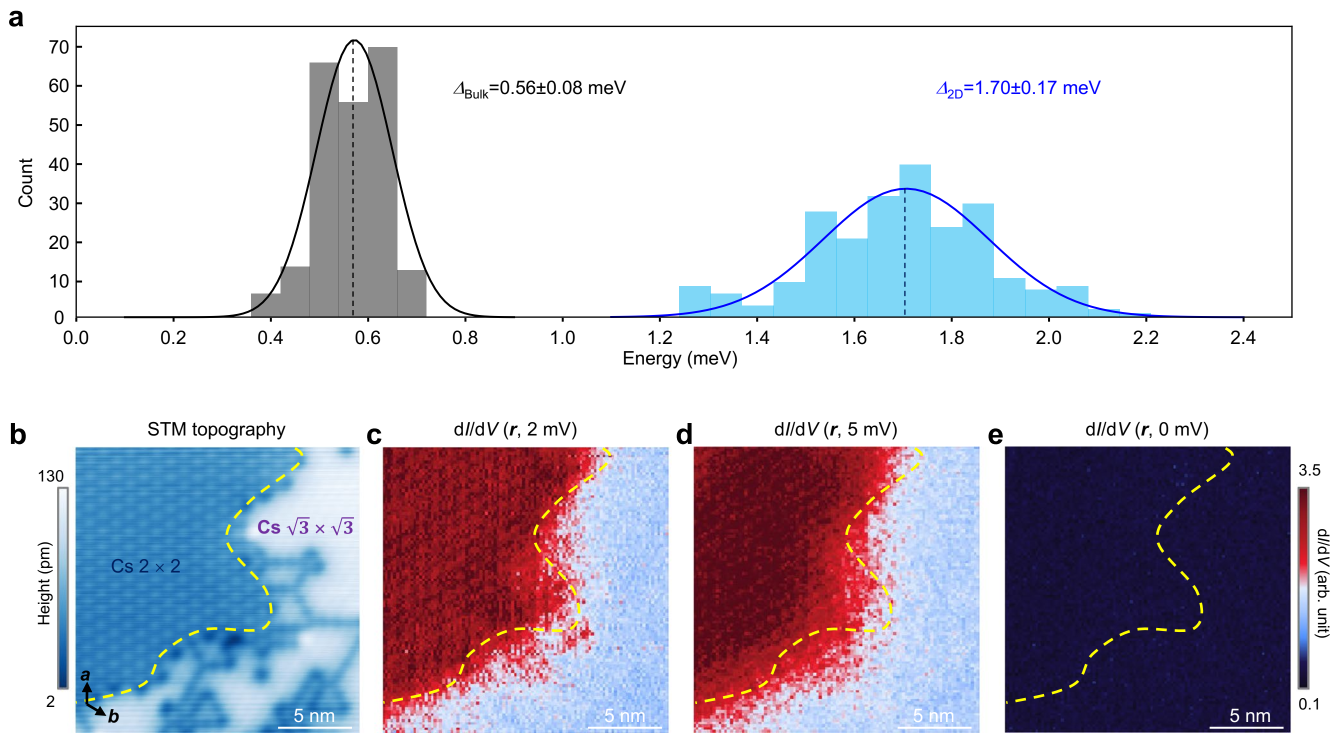

Extended Data Fig. 1 | Statistical analysis and real-space distribution of emergent energy gap Δ_{2D} on the 2×2 ordered Cs surfaces. a, Histograms of Δ_{bulk} and Δ_{2D}, fitted by normal distributions, showing the averag values of Δ_{2D} = 1.70 meV, Δ_{bulk} = 0.56 meV. **b**-**e**, STM topography of a boundary region consisting of both 2×2 and √3×√3R30°reconstructions (**b**) and three dI/dV maps at 2 mV (**c**), 5 mV (**d**), and 0 mV (**e**), showing that the electronic states with Δ_{2D} and P_{2D} only distribute on 2×2 ordered regions. Yellow dashed curves represent the boundary of the two regions. For all dI/dV data, V_{set} = 100 mV, I_t = 3 nA, V_{mod} = 0.1 mV.

https://doi.org/10.1038/s41565-025-01940-1

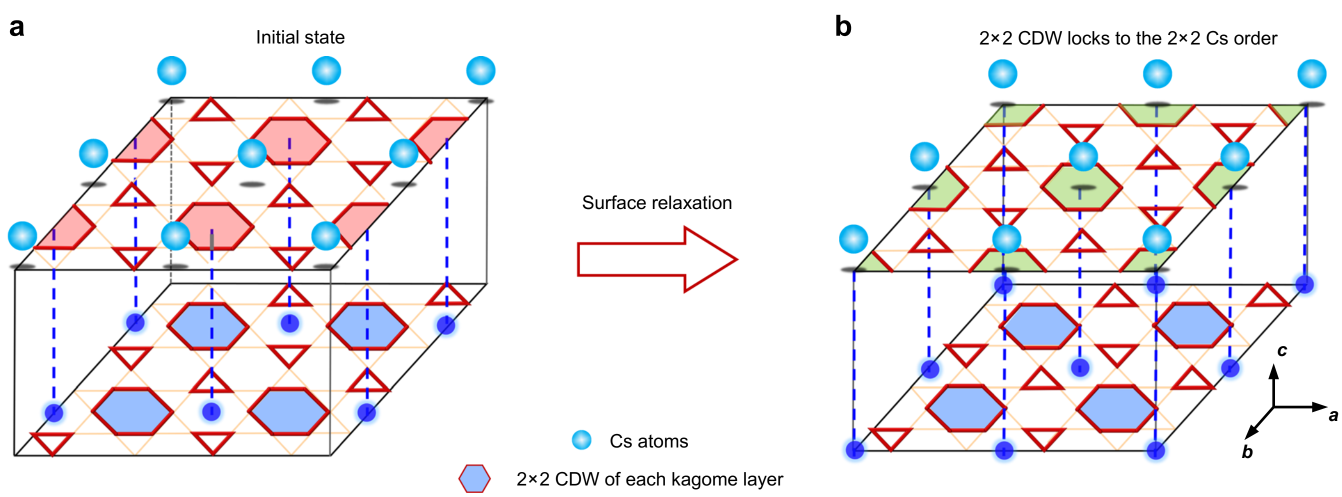

Extended Data Fig. 2 | Calculated stacking fault of CDW phases in CsV_3Sb_5 crystal with 2×2 Cs ordered surfaces before and after relaxation. Calculated stacking fault of CDW phases in CsV_3Sb_5 crystal with 2×2 Cs ordered surfaces before (**a**) and after (**b**) surface relaxation, showing that the inverse star of David pattern of 2×2 CDW in the top kagome layer will shift, following the 2×2 Cs atom sites while the inverse star of David pattern of 2×2 CDW in the second kagome layer remains unchanged.

https://doi.org/10.1038/s41565-025-01940-1

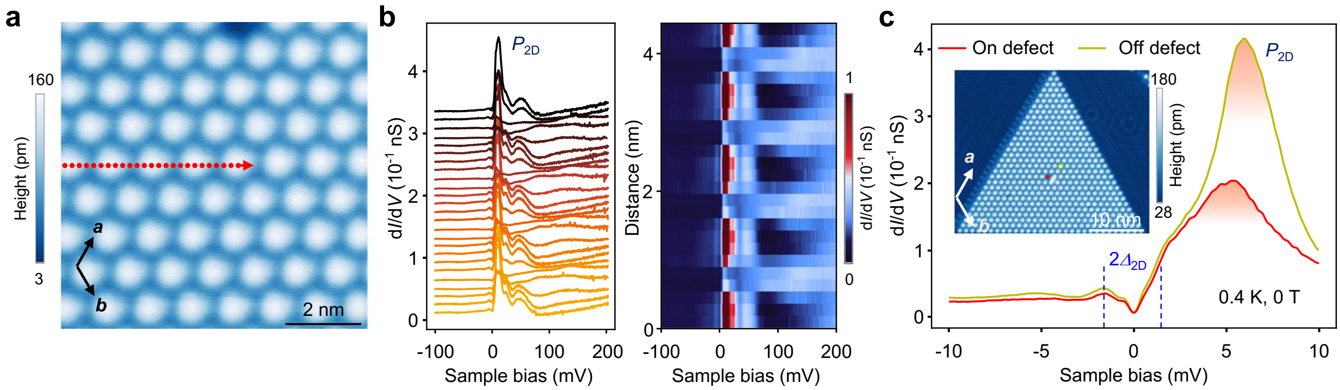

Extended Data Fig. 3 | Localized nature of P_{2D}. **a**, STM topography of a typical 2×2 Cs reconstruction. **b**, Waterfall (left) and intensity plot (right) of a dI/dV linecut along the dots and red arrow in (**a**), showing that the resonance peak P_{2D} is localized at each Cs atom of 2×2 Cs ordered surfaces. V_{set} = 100 mV, I_t = 1 nA, V_{mod} = 0.5 mV. **c**, The dI/dV spectra obtained on (red) and off (yellow) a vacancy in the 2×2 Cs triangle (inset STM topography), respectively, showing that P_{2D} is significantly suppressed at the vacancy site while the Δ_{2D} show little changes. V_{set} = 50 mV, I_t = 1.5 nA, V_{mod} = 0.15 mV.

https://doi.org/10.1038/s41565-025-01940-1

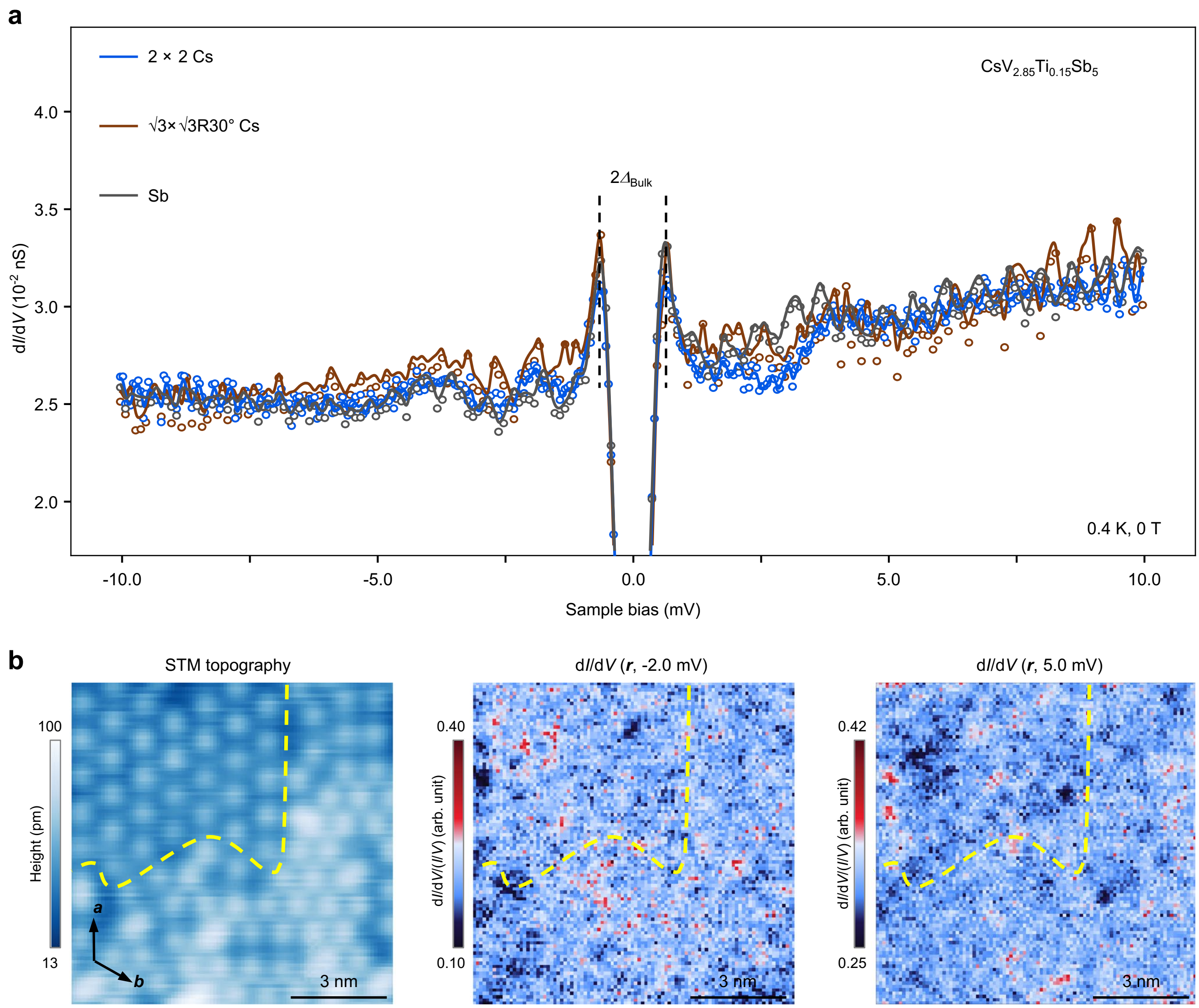

Extended Data Fig. 4 | Absence of quasi-2D superconductivity at the 2×2 ordered Cs surface in $CsV_{2.85}Ti_{0.15}Sb_5$. a, Spatially-averaged dI/dV spectra over the 2×2, √3×√3R30° ordered Cs and Sb surface regions, respectively, showing that only the bulk superconducting gap is observed on all surfaces. There is no additional energy gap at low energies for the 2×2 ordered Cs surface. **b**, STM topography, dI/dV (***r***, -2 mV) and dI/dV (***r***, 5 mV) of a boundary region between 2×2 and √3×√3R30° Cs ordered surfaces, showing there is no differnece in density of states between two surfaces (V_{set} = 100 mV, I_t = 3 nA, V_{mod} = 0.1 mV).

 https://doi.org/10.1038/s41565-025-01940-1

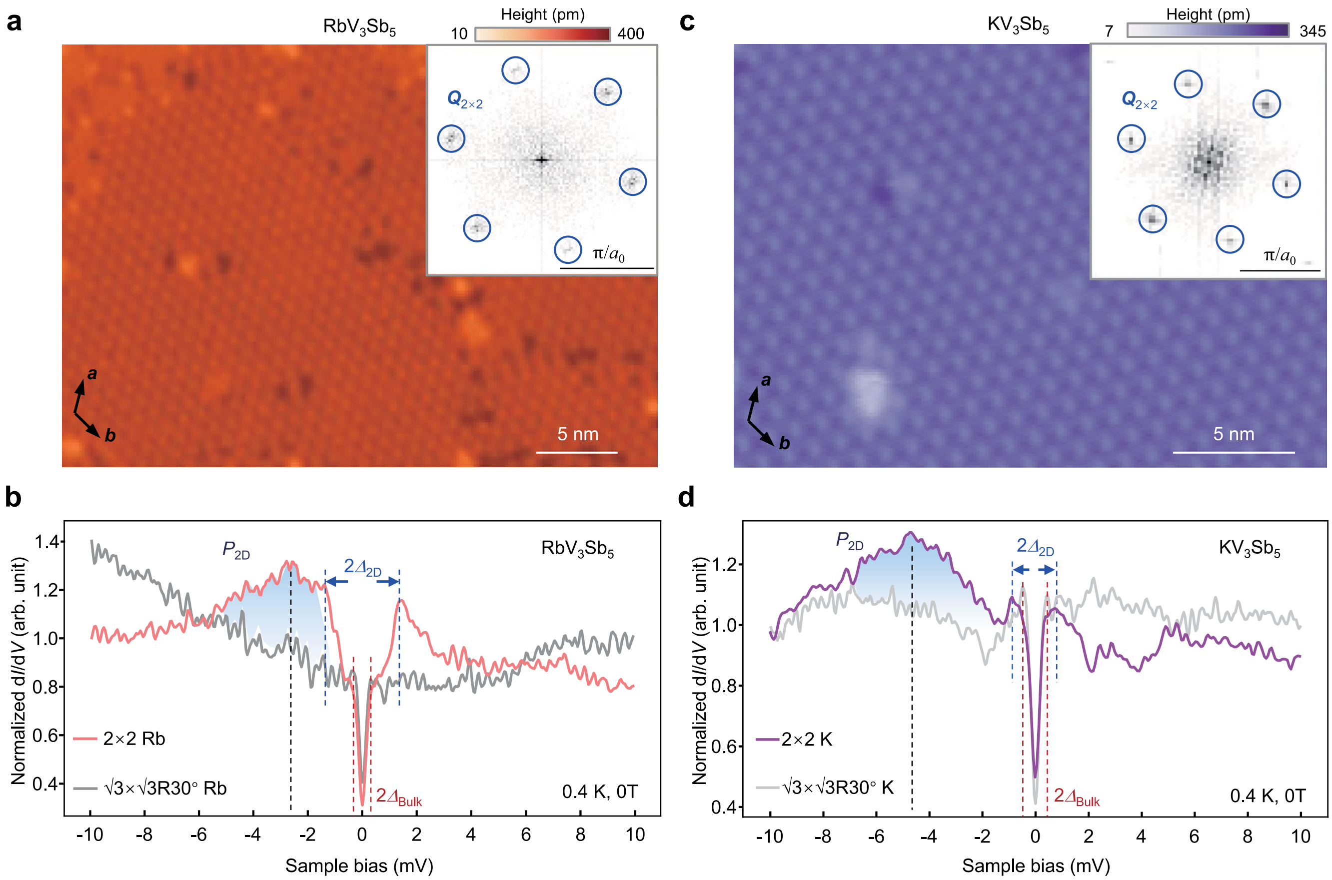

Extended Data Fig. 5 | Emergent low-energy gap and incipient bound state on the 2×2 alkali ordered surface of AV_3Sb_5 (A = Rb, K). a, The STM topography showing the 2×2 Rb ordered surface region of RbV_3Sb_5. V_{set} = 900 mV, I_t = 50 pA. **b**, Spatially-averaged dI/dV spectra obtained at the 2×2 Rb ordered surface region of RbV_3Sb_5, showing the emergence of a new quasi-2D superconducting gap Δ_{2D} with a size of ~1.4 meV and a pronounce peak at -2.8 mV (P_{2D}). **c**, The STM topography showing the 2×2 K ordered surface region of KV_3Sb_5. V_{set} = 900 mV, I_t = 50 pA. **d**, Spatially-averaged dI/dV spectra obtained at the 2×2 K ordered surface region of KV_3Sb_5, showing the emergence of a new quasi-2D superconducting gap Δ_{2D} with a size of ~0.8 meV and a pronounced peak at -4.7 mV (P_{2D}). The spectrum is normalized with respect to the average value. For all dI/dV data, V_{set} = 100 mV, I_t = 3 nA, V_{mod} = 0.1 mV.